



ÉCOLE POLYTECHNIQUE FÉDÉRALE DE LAUSANNE

ME-474 Numerical Flow Simulation

ASSESSMENT 2 - GROUP 5



Teo HALEVI, SCIPER: 329561
Selim SHERIF, SCIPER: 346035
Roy TURK, SCIPER: 345573
Jan ZGRAGGEN, SCIPER: 344351

Contents

1	Introduction	3
1.1	Context and goals of the study	3
1.2	Type of analysis and methodology	4
2	Geometric modeling and hypotheses	5
2.1	Presentation of the geometry	5
2.2	Unit system	5
2.3	Characteristic dimensions	5
2.4	Symmetry and periodicity of the problem	6
2.5	Geometrical space	6
3	Physical modeling and hypotheses	7
3.1	Physical behavior	7
3.2	Fluid properties	7
3.3	Turbulent flow modeling	7
4	Boundary conditions, external forces, initial conditions	8
4.1	Boundary conditions	8
4.2	External forces	8
4.3	Initial conditions	8
5	Computational mesh and convergence study	9
5.1	Mesh type	9
5.2	Cell type	9
5.3	Size and number of cells	9
5.4	Inflation layer	11
5.5	Results on the coarsest mesh	11
5.6	Results on the finest mesh	13
5.7	Results for all meshes	14
5.8	Estimation of the relative error	16
5.9	Choice of the final mesh	17
6	Numerical methods	19
6.1	Spatial discretization method	19
6.2	Type of simulation	19
6.3	Solution options	20
6.4	Computed quantities	20
7	Results	21

8 Analysis and conclusions	24
8.1 Summary of calculated results	24
8.2 Relevance and accuracy of the results	24
8.3 Conclusion	24
8.4 Recommendations	24

1 Introduction

1.1 Context and goals of the study

The present study aims to examine how the flying height of an aircraft wing influences its aerodynamic characteristics, namely the lift and drag coefficients.

This investigation is motivated by the operational requirements of Canadair aircraft, such as the Canadair CL-415, which are deployed in aerial firefighting missions. These aircraft routinely execute flights at low altitudes, either to discharge fire retardant agents or to refill water tanks, rendering the understanding of near-ground aerodynamic behavior crucial for both performance optimization and operational safety.



Fig. 1.1 | Italian CL-415 drops water on a fire [1]

Accordingly, the present work focuses on investigating the airflow and aerodynamic characteristics of the selected wing section. According to a compilation by the Applied Aerodynamics Group at the University of Illinois at Urbana-Champaign, the wing under consideration employs the NACA 4417 airfoil [2]. The cross-sectional geometry of this airfoil is depicted in Figure 1.2.

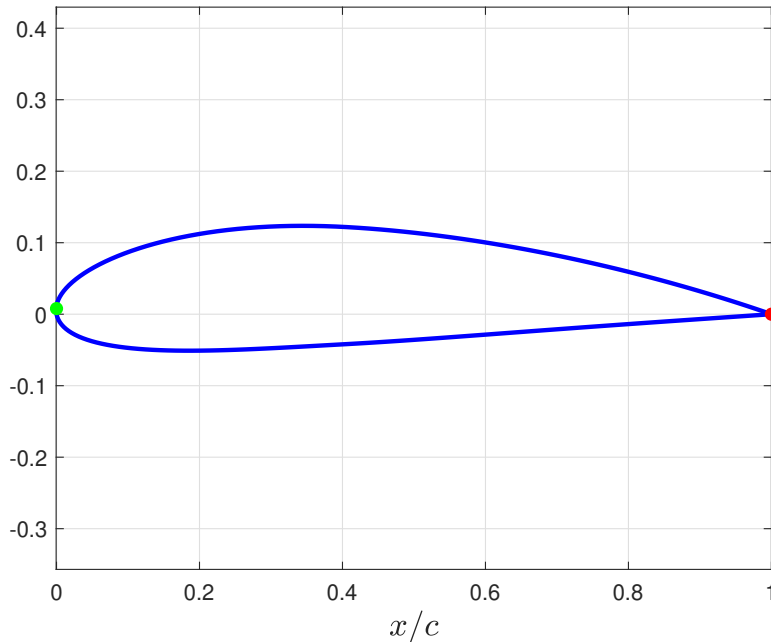


Fig. 1.2 | NACA 4417 airfoil, with the chord length denoted by c . The airflow direction is indicated from left to right, and the leading edge is highlighted by a green marker, while the trailing edge is indicated by a red marker.

1.2 Type of analysis and methodology

The fluid simulations in this study were conducted using ANSYS Fluent 2023 R1. The geometry and computational domain were created in Space Claim and subsequently transferred to Fluent Meshing via ANSYS Workbench. The integration within ANSYS Workbench facilitates task automation and enables the efficient study of multiple parameters simultaneously, streamlining the overall workflow.

2 Geometric modeling and hypotheses

2.1 Presentation of the geometry

The geometry under investigation is illustrated in Figure 1.2, which depicts the NACA 4417 airfoil. This profile belongs to the well-known NACA four-digit series, wherein the first digit (4) specifies the maximum camber as 4% of the chord, the second digit (4) indicates the location of the maximum camber at 40% of the chord length from the leading edge, and the final two digits (17) designate a maximum thickness of 17% of the chord. For the purposes of this study, a chord length of one meter was employed to define the geometry, and the distance to the ground is expressed as a dimensionless quantity h/c , where h denotes the vertical distance from the ground and c is the chord length.

The dimensions of the computational domain have been determined in accordance with the guidelines presented by Win *et al.* (2021) [3], thereby ensuring that they do not exert a measurable influence on the aerodynamic coefficients.

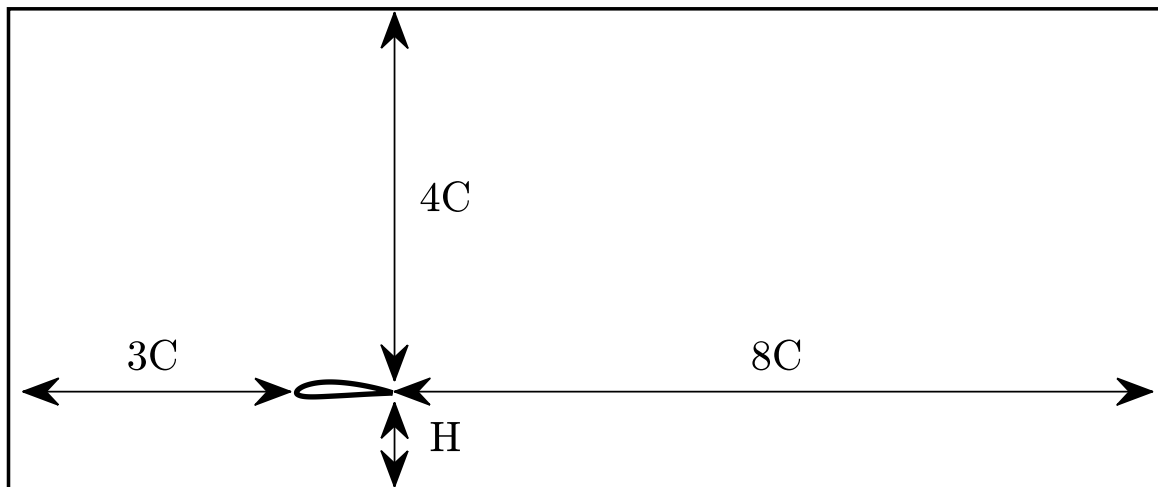


Fig. 2.3 | Computational domain dimensions, C represents the chord length and H the height to the ground.

2.2 Unit system

In this study, the Millimeter-Newton-Second (MNS) system of units was employed for all quantitative analyses. Within this framework, lengths are measured in millimeters (mm), forces in Newtons (N), and time in seconds (s).

2.3 Characteristic dimensions

The airfoil under investigation possesses a chord length c of 1 m. The aerodynamic performance is evaluated at two distinct angles of attack, specifically 4° and 6°, to assess behavior under varying inclination conditions. Additionally, the study explores the effects of ground proximity by varying the ratio h/c . The values of h/c considered in this analysis are 1, 0.8, 0.6, 0.4, 0.2, and 0.1. This range of ratios enables a comprehensive examination of the influence of vertical distance on the aerodynamic coefficients, thereby facilitating a thorough understanding of the airfoil's performance in ground proximity scenarios.

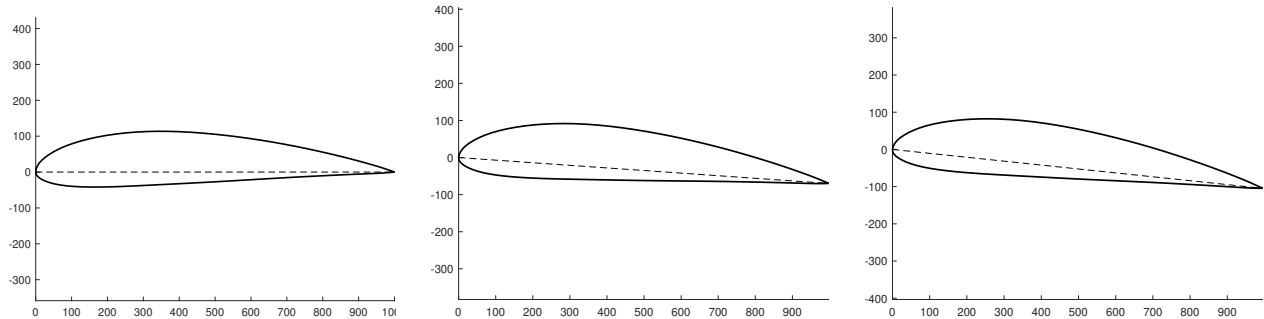


Fig. 2.4 | Visualization of the airfoil at 0° (reference), 4° , and 6° angles of attack, illustrating the different configurations studied in the analysis.

2.4 Symmetry and periodicity of the problem

The present analysis does not incorporate any symmetry or periodicity boundary conditions, as the airfoil under investigation is inherently asymmetric.

2.5 Geometrical space

The simulation is conducted within a two-dimensional (2D) spatial framework, focusing exclusively on a cross-sectional representation of the airfoil. This approach is justified, as analyzing a single cross-section sufficiently captures the primary aerodynamic characteristics without the need for three-dimensional modeling. Consequently, a 2D analysis effectively determines the aerodynamic coefficients relevant to ground proximity scenarios while optimizing computational efficiency.

3 Physical modeling and hypotheses

3.1 Physical behavior

The physical modeling of this study is predicated on the assumption that the working fluid is air, treated as a Newtonian fluid, wherein the viscous stresses are linearly related to the strain rates. Under the given operational conditions, the flow is assumed to be incompressible, as the corresponding Mach number remains sufficiently low to render compressibility effects negligible. Furthermore, the analysis excludes heat transfer, multiphase flow, and combustion phenomena, thereby concentrating on single-phase, isothermal flow dynamics around the airfoil.

3.2 Fluid properties

The airfoil is modeled to travel at a velocity of 30 m/s relative to the fluid. To streamline the analysis, a change of reference frame is applied, rendering the airfoil stationary while the fluid flows past it at the same velocity of 30 m/s.

The air density ρ is set to 1.23 kg/m^3 , and the dynamic viscosity μ is defined as $1.81 \times 10^{-5} \text{ Pa}\cdot\text{s}$. These values are consistent with standard atmospheric conditions at sea level and are critical in determining the Reynolds number, which is expressed as

$$Re = \frac{\rho u L}{\mu} = 2.04 \times 10^6 \quad (3.1)$$

where Re denotes the Reynolds number, ρ the fluid density, u the free-stream velocity, L the characteristic length, and μ the dynamic viscosity.

3.3 Turbulent flow modeling

The flow is characterized by a high Reynolds number, representative of practical aerodynamic conditions such as those encountered around airfoils. The $k - \omega$ turbulence model is employed due to its effectiveness in resolving both the near-wall region and free-stream turbulence. To ensure accurate predictions, the mesh is designed with a fine resolution in the boundary layer, maintaining $y^+ < 1$ to fully capture the viscous sub-layer and achieve reliable lift and drag predictions.

4 Boundary conditions, external forces, initial conditions

4.1 Boundary conditions

The boundary conditions applied to the computational domain are as follows:

- **Inlet:** A velocity boundary condition was applied at the inlet, set to **30 m/s**, representing the free-stream velocity entering the domain. This ensures consistent and realistic upstream flow conditions.
- **Outlet:** A pressure outlet boundary condition was applied at the outlet, set to **0 Pa** gauge pressure. This allows smooth exit of flow disturbances and prevents artificial reflections, ensuring a realistic downstream environment.
- **Ground:** A no-slip wall boundary condition was applied to the ground to model the aerodynamic interaction with the airfoil. This condition captures the ground effect accurately, which is critical for simulating near-ground aerodynamic behavior.
- **Top:** A symmetry boundary condition was applied at the top of the computational domain. This choice was made to represent the undisturbed free-stream flow far from the airfoil. The symmetry condition ensures:
 - Zero normal velocity and frictionless tangential flow, mimicking the physical behavior of an open boundary.
 - Placement of the boundary sufficiently far from the airfoil prevents interference with the flow field, maintaining solution accuracy.
 - A balance of physical realism and computational efficiency, avoiding unnecessary complexity.
- **Airfoil:** A no-slip wall boundary condition was applied to the airfoil surface to model the viscous effects of airflow. This ensures accurate boundary layer development and reliable computation of aerodynamic forces.

4.2 External forces

External forces are excluded from the analysis.

4.3 Initial conditions

The simulation is performed under steady-state conditions, thereby eliminating the need for initial transient states.

5 Computational mesh and convergence study

5.1 Mesh type

The computational domain is discretized using a hybrid meshing approach, comprising both structured and unstructured mesh regions to optimize accuracy and computational efficiency. A structured mesh is employed in the bulk of the enclosure, where the flow is relatively uniform and less complex, facilitating efficient numerical calculations and ensuring grid regularity. In contrast, an unstructured mesh is utilized in the vicinity of the airfoil, where the flow exhibits significant gradients and complex aerodynamic interactions. This localized unstructured meshing allows for finer grid resolution and greater flexibility in capturing intricate flow features.

5.2 Cell type

The computational mesh utilizes two-dimensional quadrilateral elements throughout the entire domain. Quadrilateral cells are selected for their ability to accurately capture complex flow features and streamline patterns around the airfoil. Additionally, they offer superior numerical stability and faster convergence compared to triangular elements, enhancing the efficiency and reliability of the aerodynamic simulations.

5.3 Size and number of cells

The mesh configuration is detailed as follows

- **Body of influence edges:** a uniform edge sizing is imposed on the region surrounding the airfoil and its vicinity. (Zone A)

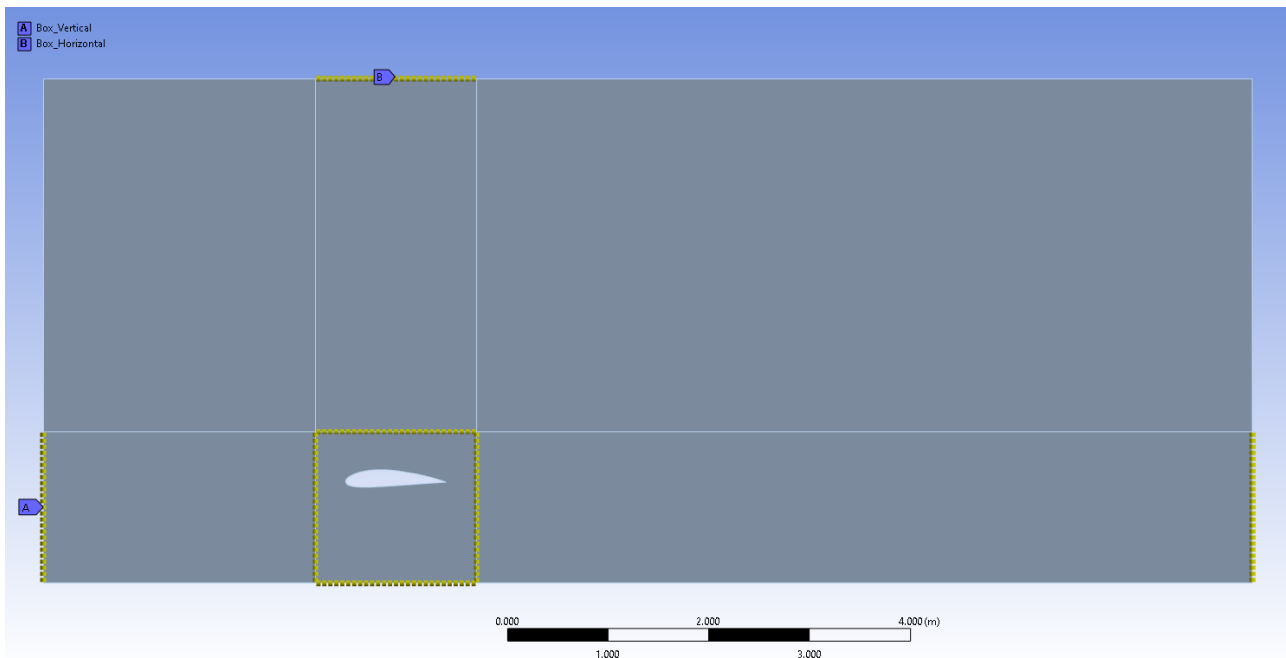


Fig. 5.5 | Edge sizing applied to the body of influence around the airfoil. (Zone A)

- **Vertical and horizontal edges:** edge sizings are systematically applied to all remaining boundaries with a bias factor of 4.0. The element size is selected to ensure uniform cell dimensions at

the interfaces between the top and bottom regions, as well as at the intersections among the left, middle, and right sections of the computational mesh. (Zone B)

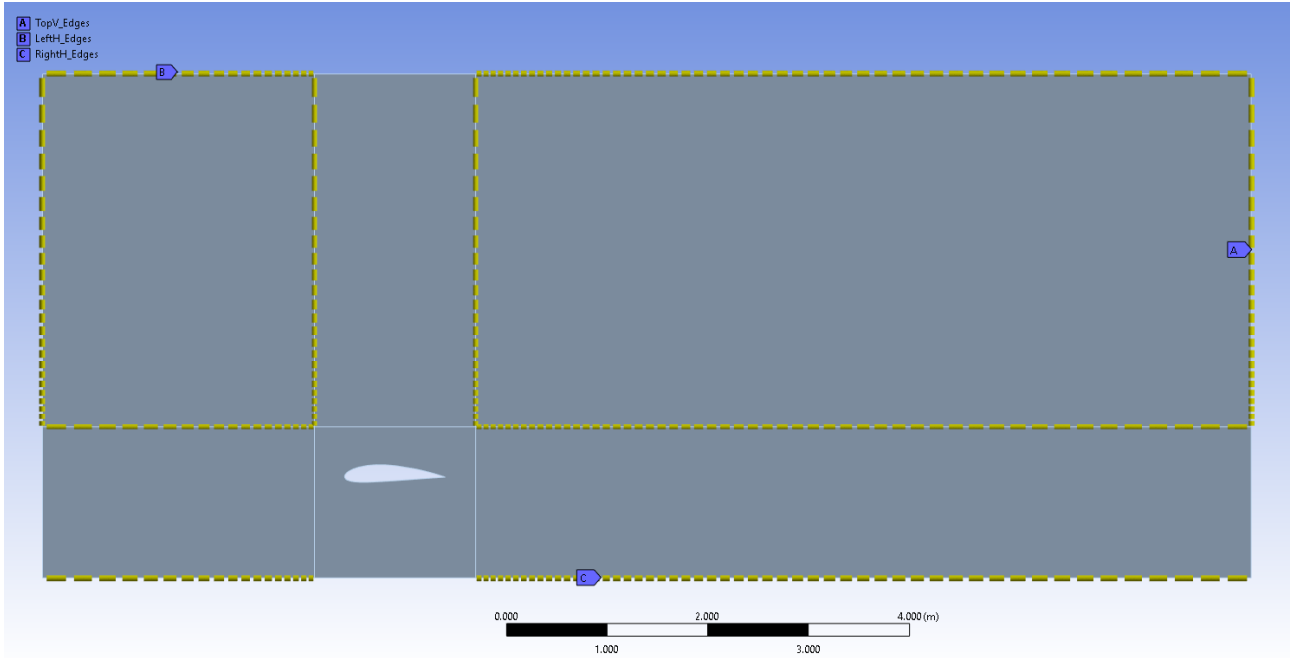


Fig. 5.6 | Edge sizing applied to remaining edges. (Zone B)

- **Airfoil edge:** a uniform edge sizing is applied to the airfoil, consistent with the sizing employed in the body of influence region.

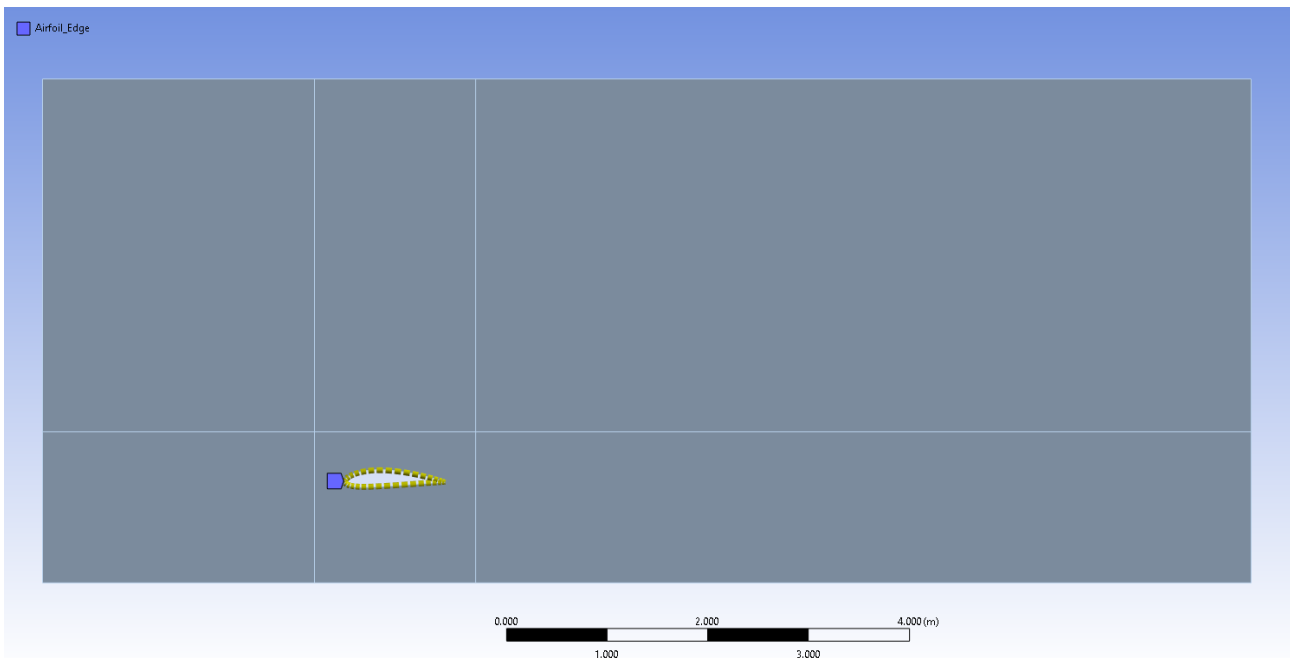


Fig. 5.7 | Edge sizing applied on airfoil surface.

The element size in Zone A is decreased with a factor of $\sqrt{2}$, this allows us to have a significant increase in the number of cells between each mesh for the convergence study. A summary of the various mesh configurations employed in this study is presented Tab.5.1.

Mesh number	Element size (A) [mm]	Element size (B) [mm]	Number of cells	Skewness	Orthogonal quality
1	60	150	5582	0.0572	0.928
2	42	105	10851	0.0410	0.956
3	30	75	20161	0.0313	0.974
4	20	50	43765	0.0218	0.987
5	17.5	43.75	56886	0.0198	0.990
6	15	37.5	76988	0.0173	0.992

Table 5.1 | Meshes employed for convergence study.

5.4 Inflation layer

To accurately capture the boundary layer effect an inflation layer is incorporated into the mesh design. The required parameters are computed with [4]. We obtain a total of 25 layers with a first layer height of 0.0242 mm and a growth rate of 1.24.

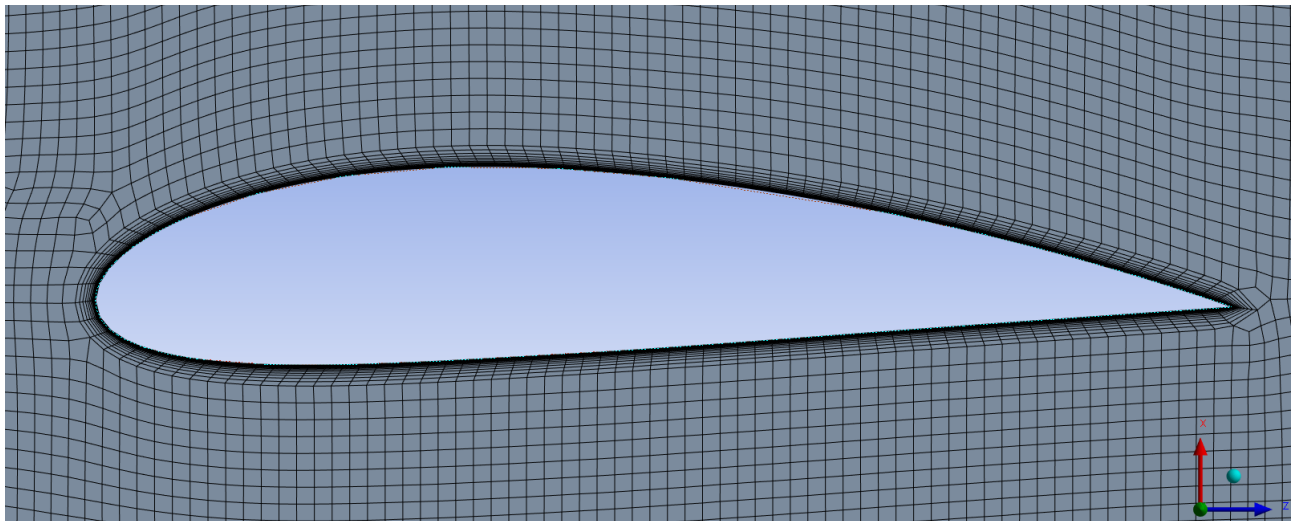


Fig. 5.8 | Close-up of inflation layer around airfoil boundary.

5.5 Results on the coarsest mesh

A view of the coarsest mesh is shown in Fig.5.9, and a close-up of the region around the airfoil in Fig.5.10. The coarsest mesh serves as the baseline for the convergence study, allowing us to evaluate the impact of grid refinement on the accuracy of aerodynamic coefficients.

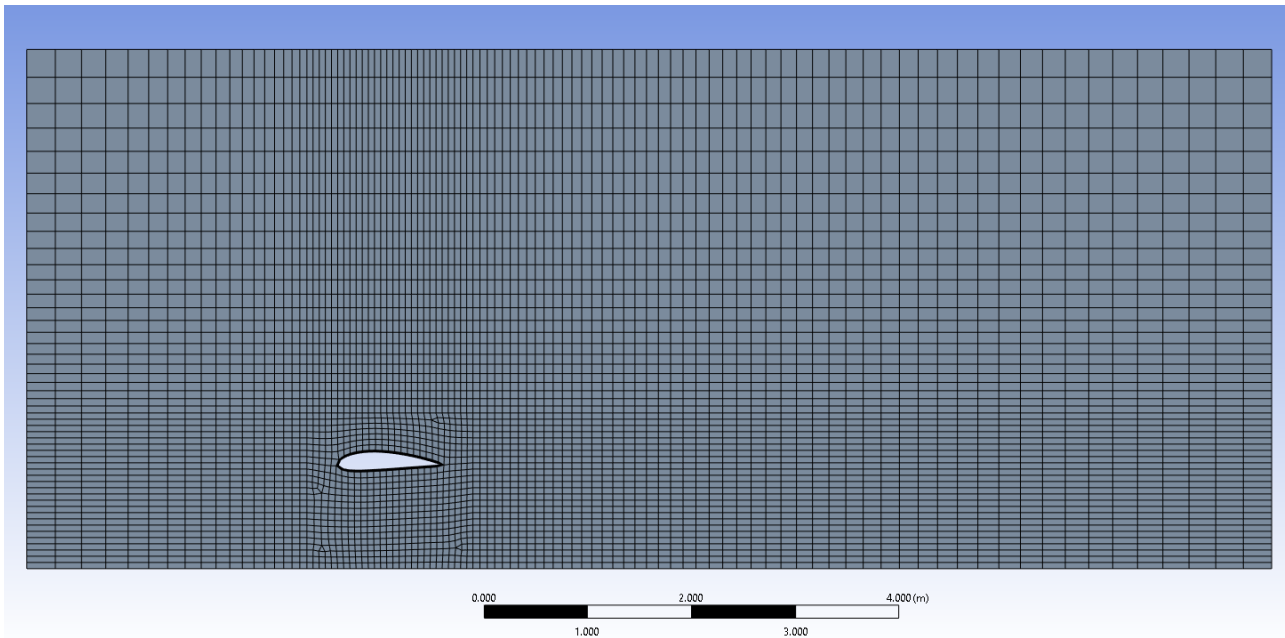


Fig. 5.9 | Overview of the coarsest mesh showing the airfoil within the domain and the surrounding quadrilateral elements, highlighting the global mesh structure.

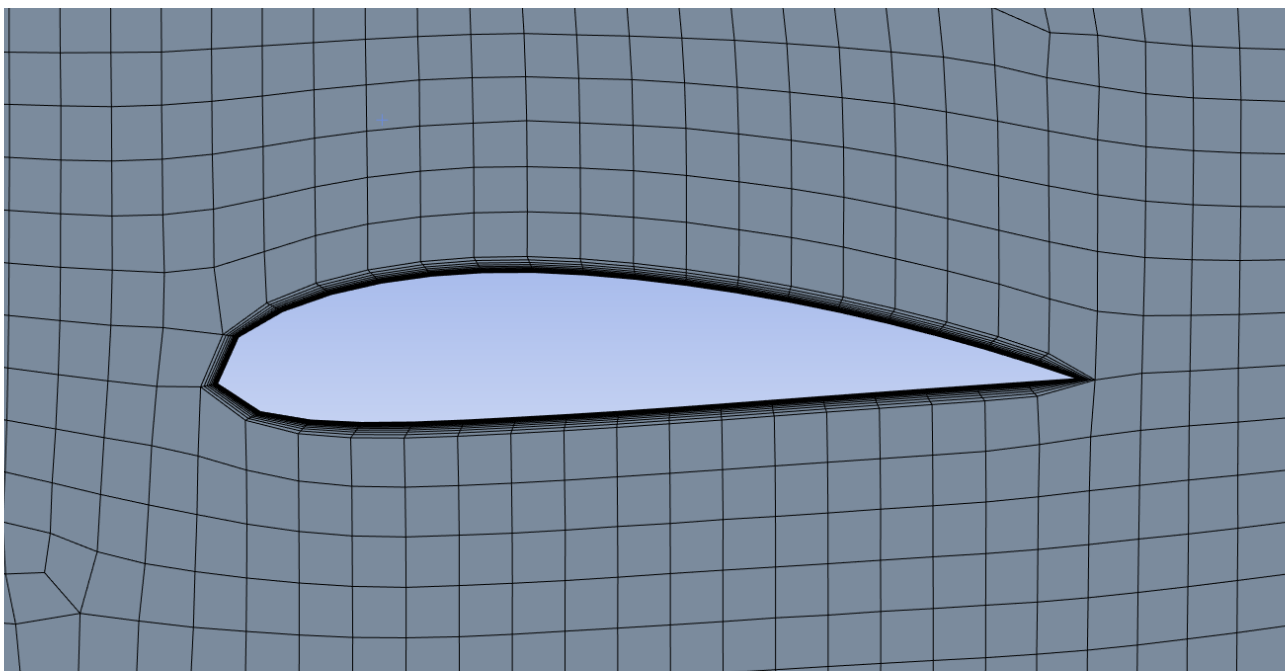


Fig. 5.10 | Close-up view of the mesh near the airfoil, illustrating the refinement of grid elements around the airfoil surface to capture flow features accurately.

The results for the lift and drag coefficients with the coarsest mesh are shown in Tab.5.2.

Mesh number	C_L	C_D	L [N]	D [N]
1	0.404	0.0316	222.9	17.42

Table 5.2 | Aerodynamic results obtained for Mesh 1, including lift and drag coefficients, as well as the corresponding lift and drag forces.

5.6 Results on the finest mesh

The finest mesh, shown in Fig.5.11, exhibits significantly greater resolution compared to the coarsest mesh. While the coarsest mesh employs a uniform distribution of larger quadrilateral elements, the finest mesh features smaller cells with more pronounced refinement around the airfoil surface and in regions of high flow gradients, such as the boundary layer. This finer discretization ensures a higher level of accuracy in capturing the intricate flow features and aerodynamic phenomena, albeit at a greater computational cost.

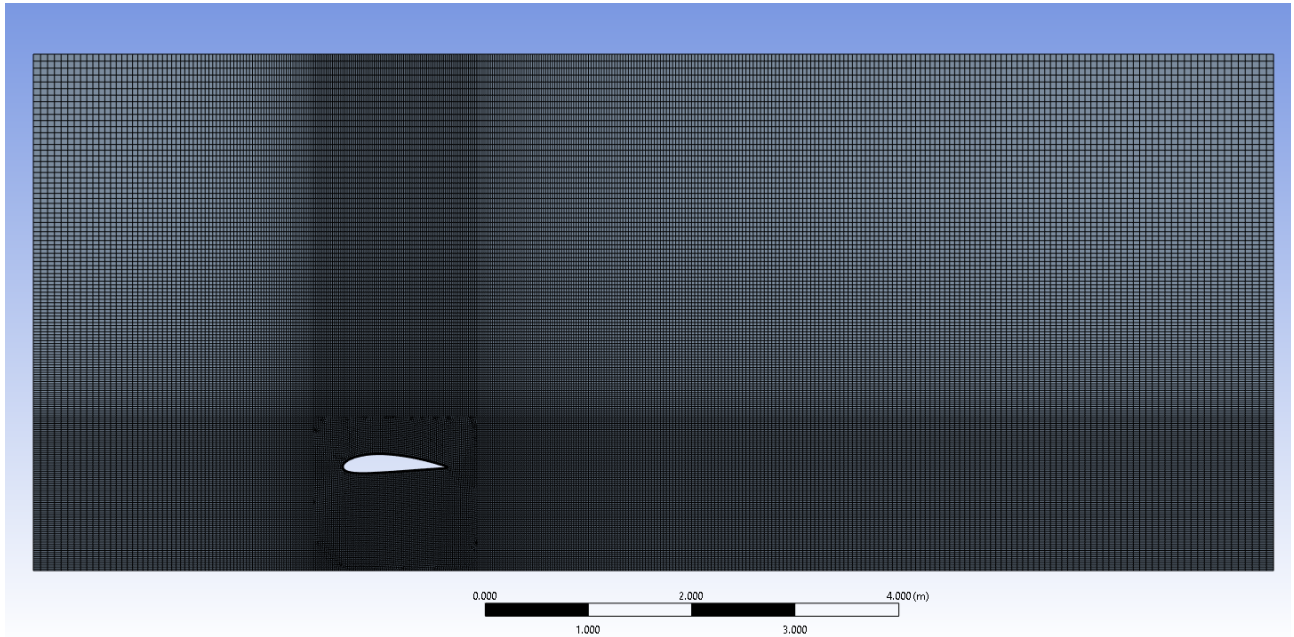


Fig. 5.11 | Overview of the finest mesh showing the airfoil within the domain and the surrounding quadrilateral elements, highlighting the global mesh structure.

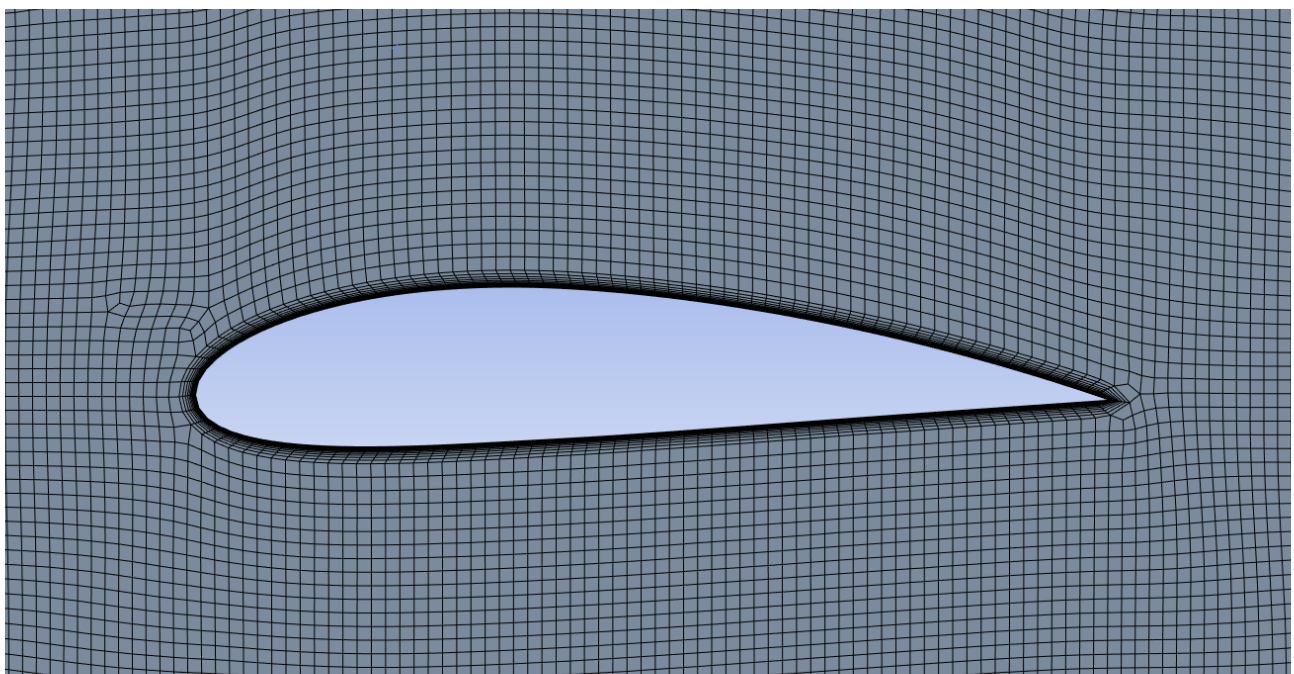


Fig. 5.12 | Close-up view of the mesh near the airfoil, illustrating the refinement of grid elements around the airfoil surface to capture flow features accurately.

The final aerodynamic coefficients, presented in Tab.5.3, will be later used to evaluate convergence across the different meshes and guide the selection of the optimal mesh for further analysis.

Mesh number	C_L	C_D	L [N]	D [N]
6	0.449	0.0117	247.3	6.430

Table 5.3 | Aerodynamic results obtained for Mesh 6, including lift and drag coefficients, as well as the corresponding lift and drag forces.

5.7 Results for all meshes

Mesh number	Number of cells	C_L	C_D	L [N]	D [N]
1	5582	0.404	0.0316	222.9	17.42
2	10851	0.479	0.0228	263.9	12.58
3	20161	0.480	0.0180	264.8	9.915
4	43765	0.444	0.0131	244.85	7.204
5	56886	0.449	0.0121	247.3	6.646
6	76988	0.449	0.0117	247.3	6.430

Table 5.4 | Aerodynamic results for all meshes used in the convergence study, showing the number of cells, lift and drag coefficients, and the corresponding lift and drag forces for each mesh refinement.

The graph in Fig.5.13 shows the variation of the lift coefficient as a function of the number of cells in the computational mesh. As the mesh is refined, C_L initially increases significantly, indicating that finer meshes capture more accurate flow features. Beyond approximately 40,000 cells, C_L stabilizes around a value of 0.45, suggesting that further mesh refinement has a negligible impact on the computed lift coefficient.

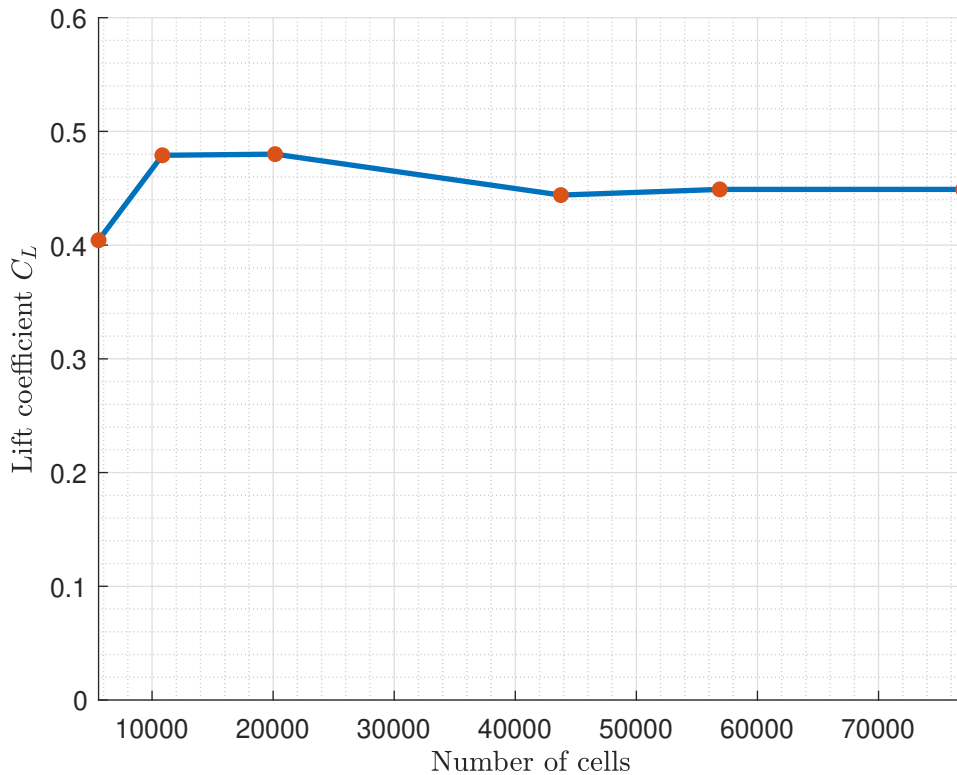


Fig. 5.13 | Convergence of the lift coefficient C_L with increasing number of cells. The lift coefficient stabilizes around $C_L = 0.45$.

Similarly, the graph of Fig.5.14 shows the variation of the drag coefficient with increasing mesh resolution. Beyond 40,000 cells, C_D stabilizes around a value of 0.01, indicating that the drag coefficient also reached convergence.

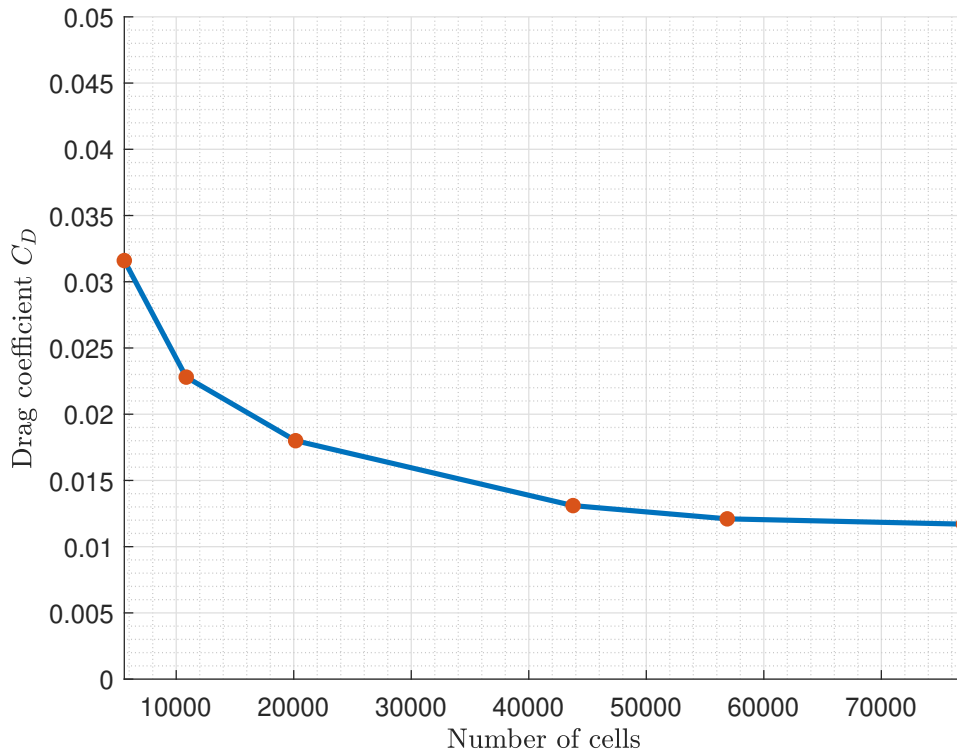


Fig. 5.14 | Convergence of the drag coefficient C_D with increasing number of cells. The drag coefficient stabilizes around $C_D = 0.01$.

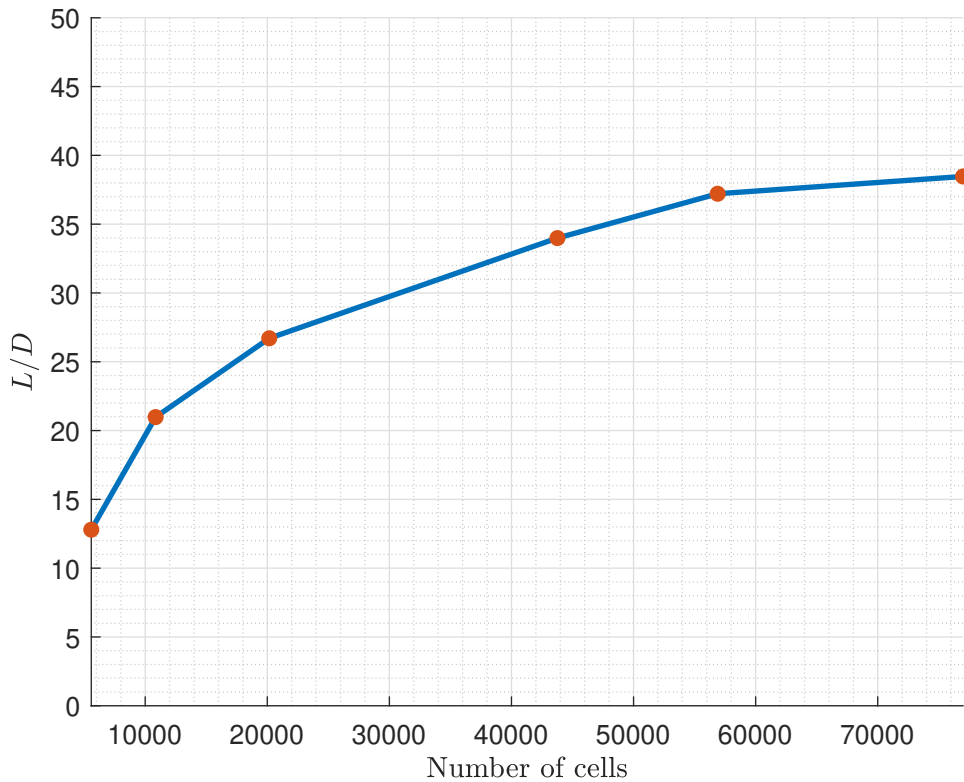


Fig. 5.15 | Convergence of the lift to drag ratio L/D with increasing number of cells.

The lift-to-drag ratio L/D represents the aerodynamic efficiency of the airfoil, indicating how much lift is generated relative to the drag. A higher ratio corresponds to better aerodynamic performance. As shown in the graph, L/D increases with mesh refinement and stabilizes beyond approximately 40,000 cells, indicating that the solution has converged with respect to mesh resolution.

5.8 Estimation of the relative error

The relative error is computed with respect to the results of the preceding mesh to assess the convergence between successive mesh refinements. The relative error is defined as

$$\varepsilon_i = \frac{\Sigma(i) - \Sigma(i-1)}{\Sigma(i)} \quad (5.2)$$

where $\Sigma(i)$ represents the solution obtained from the current mesh, and $\Sigma(i-1)$ corresponds to the coefficient from the previous mesh. This approach provides a localized measure of convergence, highlighting the incremental improvement in accuracy as the mesh resolution increases.

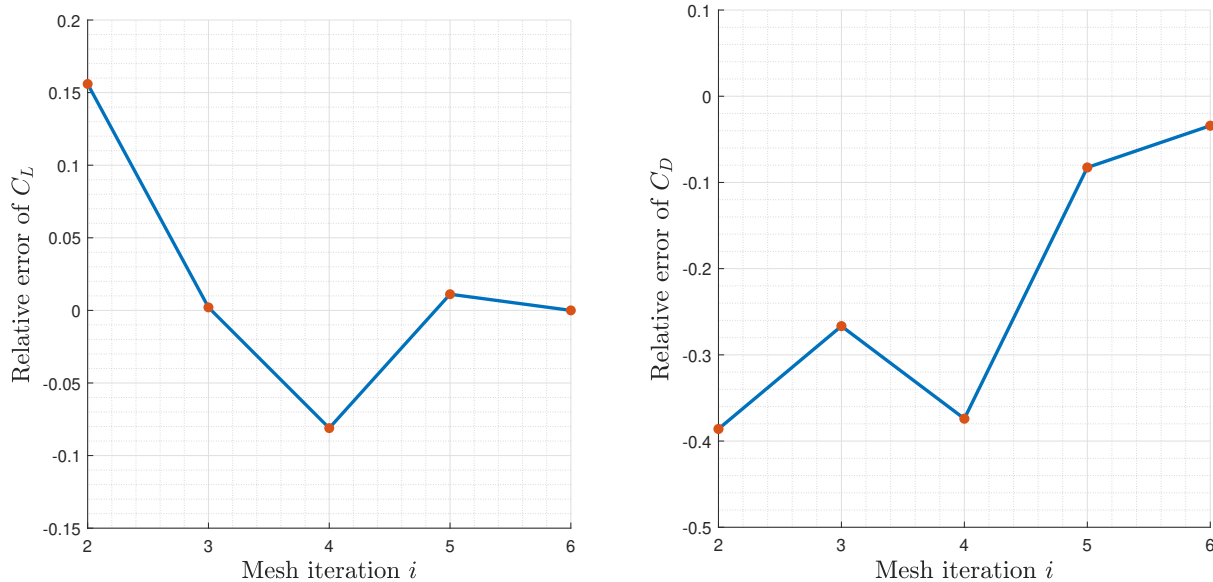


Fig. 5.16 | Relative error for lift and drag coefficients between successive mesh refinements.

The relative error graphs in Fig.5.16, confirm the same trend seen previously. The relative error for C_L and C_D becomes negligible between the fifth and sixth meshes, indicating that further refinement has little impact on solution accuracy.

The results indicate that Mesh 5 provides an optimal balance between computational efficiency and accuracy. It captures the flow physics reliably while avoiding unnecessary computational costs associated with additional refinement.

5.9 Choice of the final mesh

After conducting a convergence study across various meshes, Mesh 5 is selected as the final configuration for subsequent analysis of the airfoil's aerodynamic coefficients.

Mesh number	Element size (A) [mm]	Element size (B) [mm]	Number of cells	Skewness	Orthogonal quality
5	17.5	43.75	56886	0.0198	0.990

Table 5.5 | Properties of the final mesh selected for subsequent simulations.

The final mesh, as summarized in Tab.5.5, consists of 56,886 cells, providing sufficient resolution for the aerodynamic analysis. The skewness and orthogonal quality metrics indicate a well-distributed and structured grid, suitable for accurately capturing the flow physics around the airfoil without significant numerical artifacts.

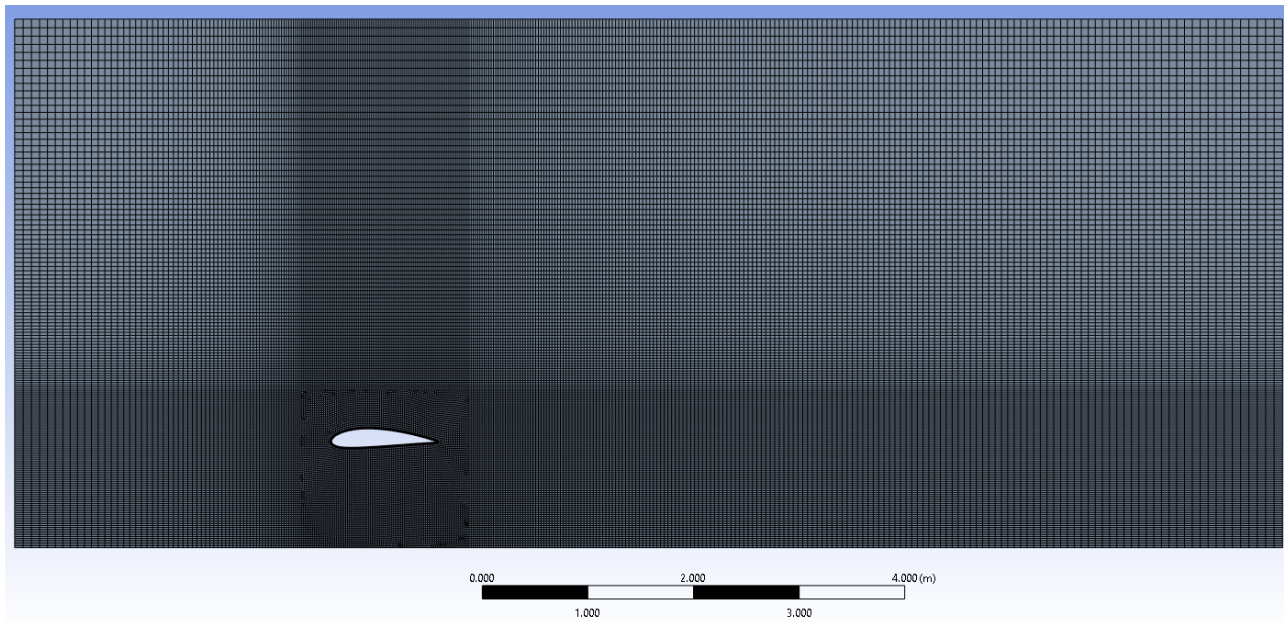


Fig. 5.17 | Overview of the final mesh showing the airfoil within the domain and the surrounding quadrilateral elements, highlighting the global mesh structure.

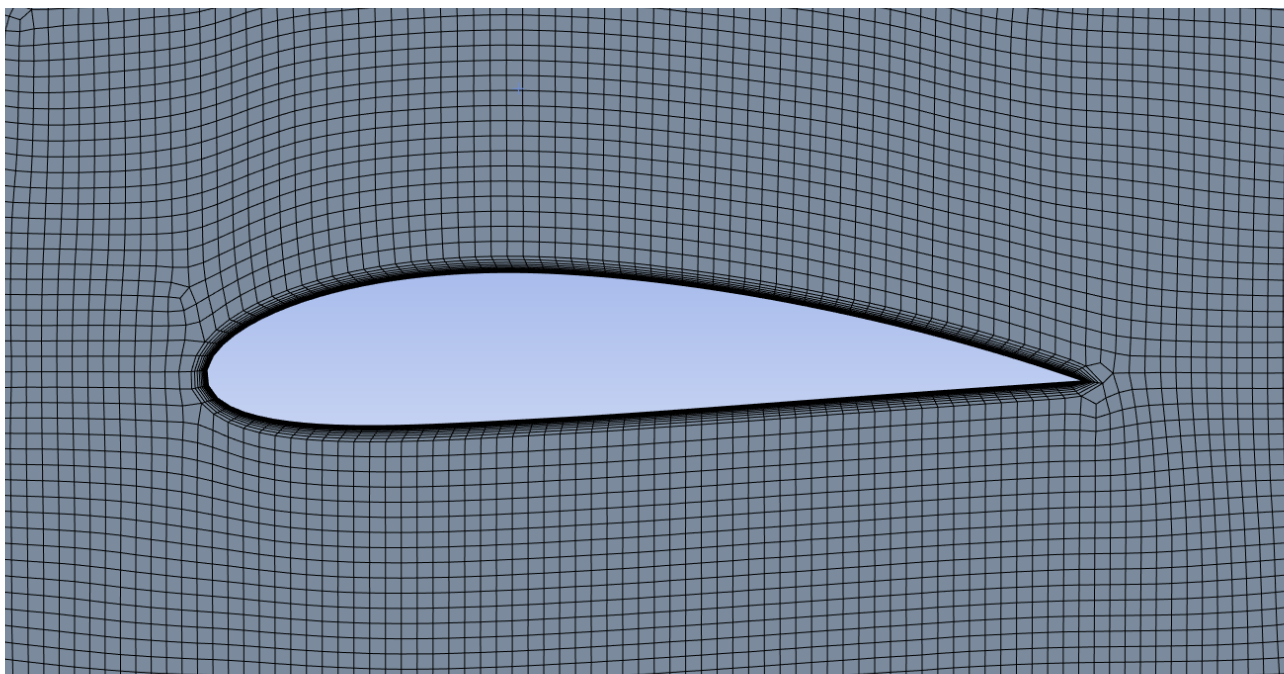


Fig. 5.18 | Close-up view of the mesh near the airfoil, illustrating the refinement of grid elements around the airfoil surface to capture flow features accurately.

6 Numerical methods

6.1 Spatial discretization method

ANSYS Fluent utilizes the finite volume method (FVM) as the default spatial discretization technique. This method involves dividing the computational domain into discrete control volumes, where the governing equations are integrated to conserve quantities such as mass, momentum, and energy.

The spatial discretization in this study is performed using the default settings. For gradient computation, the Least Squares Cell-Based method is utilized, which ensures accurate gradient evaluations even on unstructured meshes. The Second-Order Upwind scheme is applied to the pressure, momentum, turbulent kinetic energy, and specific dissipation rate equations, offering improved accuracy compared to first-order schemes by accounting for higher-order flow variations. This approach ensures better resolution of gradients and flow features, especially in regions of high shear or turbulence and maintains numerical stability. The pressure-velocity coupling is handled using the Coupled Scheme, which accelerates convergence by solving the momentum and pressure equations together.

6.2 Type of simulation

The simulation is conducted using a pressure-based solver in ANSYS Fluent, which is well-suited for incompressible and mildly compressible flows. The velocity formulation is set to absolute, ensuring that the velocity field is evaluated relative to a fixed reference frame. A steady-state simulation is performed to analyze the long-term flow behavior and achieve a solution independent of time. The turbulence model employed is the $k - \omega$ model, which is particularly effective for capturing near-wall effects and accurately resolving turbulent flow characteristics.

The variables solved for include:

1. Primary variables

- Pressure p : solved as part of the continuity and momentum equations, to ensure mass conservation across the domain.
- Velocity components (u, v): the momentum equations solve for the velocity components in the x -direction and y -direction to describe the flow field.

2. Turbulence quantities

- Turbulent kinetic energy k : represents the energy in turbulent eddies and is crucial to model turbulence effects in the flow.
- Specific dissipation rate ω : solved as part of the turbulence model, defining the rate at which turbulence dissipates.

The variables solved for in the simulation are governed by the following fundamental equations:

- **Continuity equation**

For incompressible steady flow, the continuity equation ensures mass conservation.

$$\frac{\partial u}{\partial x} + \frac{\partial v}{\partial y} = 0 \quad (6.3)$$

where u and v are the velocity components in the x - and y -directions, respectively.

- **Momentum equations**

The momentum equations describe the conservation of momentum in the flow field.

$$\rho \left(u \frac{\partial u}{\partial x} + v \frac{\partial u}{\partial y} \right) = - \frac{\partial p}{\partial x} + \mu \left(\frac{\partial^2 u}{\partial x^2} + \frac{\partial^2 u}{\partial y^2} \right) \quad (6.4)$$

$$\rho \left(u \frac{\partial v}{\partial x} + v \frac{\partial v}{\partial y} \right) = - \frac{\partial p}{\partial y} + \mu \left(\frac{\partial^2 v}{\partial x^2} + \frac{\partial^2 v}{\partial y^2} \right) \quad (6.5)$$

where ρ is the fluid density, μ the dynamic viscosity of the fluid, and p is the pressure.

- **Turbulence model equations**

The following equations are solved to model turbulence effects

$$\rho \frac{\partial k}{\partial t} + \rho u_j \frac{\partial k}{\partial x_j} = P_k - \beta^* \rho k \omega + \frac{\partial}{\partial x_j} \left[(\mu + \sigma_k \mu_t) \frac{\partial k}{\partial x_j} \right] \quad (6.6)$$

$$\rho \frac{\partial \omega}{\partial t} + \rho u_j \frac{\partial \omega}{\partial x_j} = \alpha \frac{\omega}{k} P_k - \beta \rho \omega^2 + \frac{\partial}{\partial x_j} \left[(\mu + \sigma_\omega \mu_t) \frac{\partial \omega}{\partial x_j} \right] \quad (6.7)$$

where P_k is the production of turbulent kinetic energy, μ_i is the turbulent viscosity, and $\alpha, \beta, \beta^*, \sigma_k$, and σ_ω are the model constants.

6.3 Solution options

The solution is initialized with standard Fluent hybrid initialization.

The convergence criteria are maintained at the default settings provided by ANSYS Fluent, as these settings are generally robust for a wide range of aerodynamic simulations. The numerical solution is deemed to have converged when the residuals for the continuity equation, velocity components, and turbulence model each fall below the absolute threshold of 0.001.

6.4 Computed quantities

The primary quantities of interest in this study are the lift and drag coefficients, which are derived from the lift and drag forces acting on the airfoil. The lift L and drag D forces are computed as

$$L = \int_S [-pn_y + \tau_{xy}n_x] dx \quad (6.8)$$

$$D = \int_S [-pn_x + \tau_{xx}n_x] dx \quad (6.9)$$

where τ_{xx}, τ_{xy} are the viscous stress components, and n_x, n_y are the components of the unit normal vector to the airfoil surface.

The coefficients are then obtained from

$$C_L = \frac{L}{\frac{1}{2} \rho U_\infty^2 c} \quad (6.10)$$

$$C_D = \frac{D}{\frac{1}{2} \rho U_\infty^2 c} \quad (6.11)$$

where U_∞ represents the free-stream velocity.

7 Results

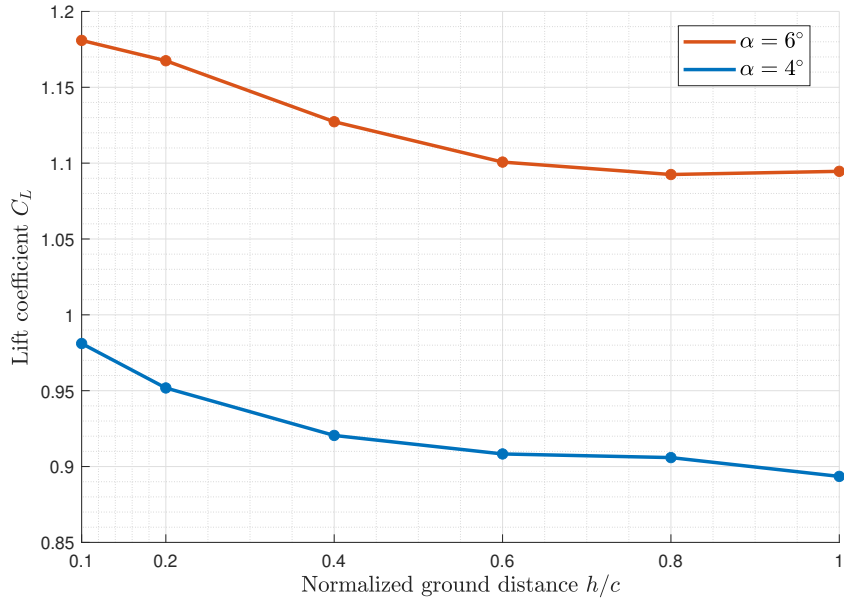


Fig. 7.19 | Variation of the lift coefficient C_L with normalized ground distance h/c for two angles of attack $\alpha = 4^\circ$ and $\alpha = 6^\circ$.

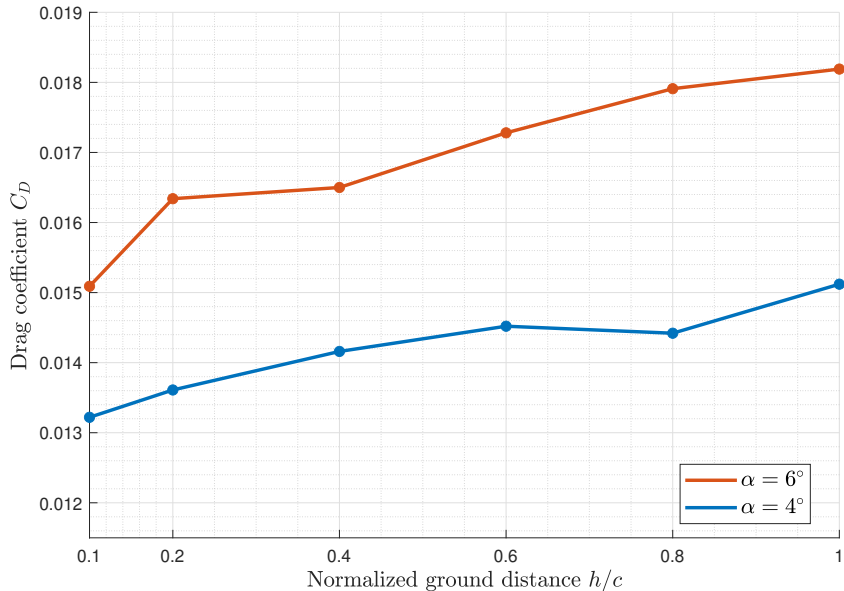


Fig. 7.20 | Variation of the drag coefficient C_D with normalized ground distance h/c for two angles of attack $\alpha = 4^\circ$ and $\alpha = 6^\circ$.

The results indicate that the lift coefficient C_L increases as the airfoil moves closer to the ground, driven by the amplified pressure differential resulting from ground proximity. At higher angles of attack, the lift coefficient is further enhanced due to stronger interactions between the airfoil and the surrounding flow field. In contrast, the drag coefficient C_D decreases with decreasing ground distance, reflecting reduced drag forces near the ground. For larger h/c values, both C_L and C_D stabilize, signifying a diminishing influence of ground effect at greater distances. Our findings exhibit similar trends to those reported by Qu *et al.* (2015), demonstrating consistent behavior of the lift and drag coefficients across different height-to-chord ratios [5].

Our numerical simulation also extracts the air pressure and velocity fields around the airfoil. These fields are given for a flight height of $h/c = 0.4$ and are shown in Fig. 7.21 and Fig. 7.22.

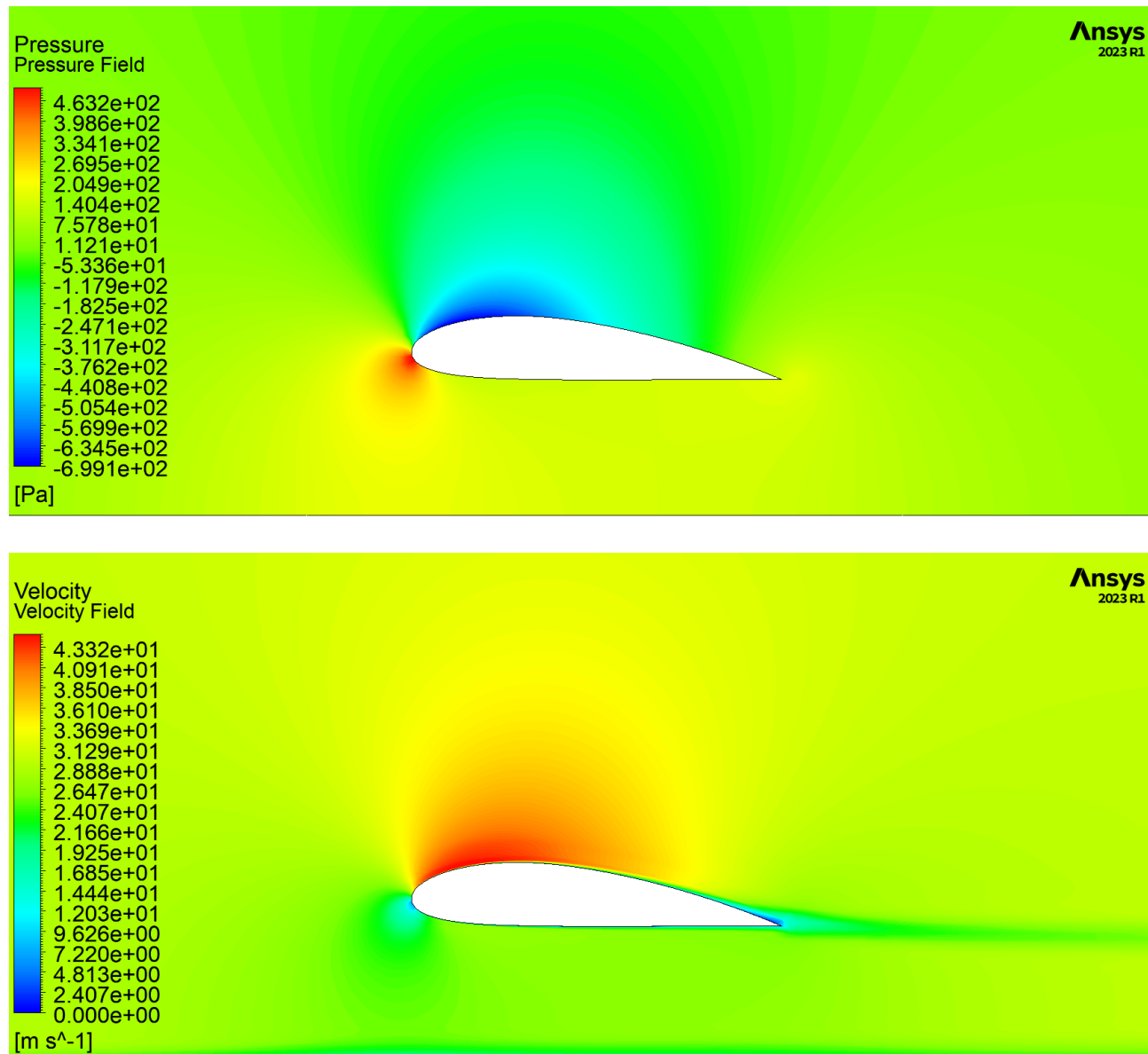


Fig. 7.21 | Contour plots of the pressure and velocity fields around the airfoil at $\alpha = 4^\circ$ and $h/c = 0.4$.

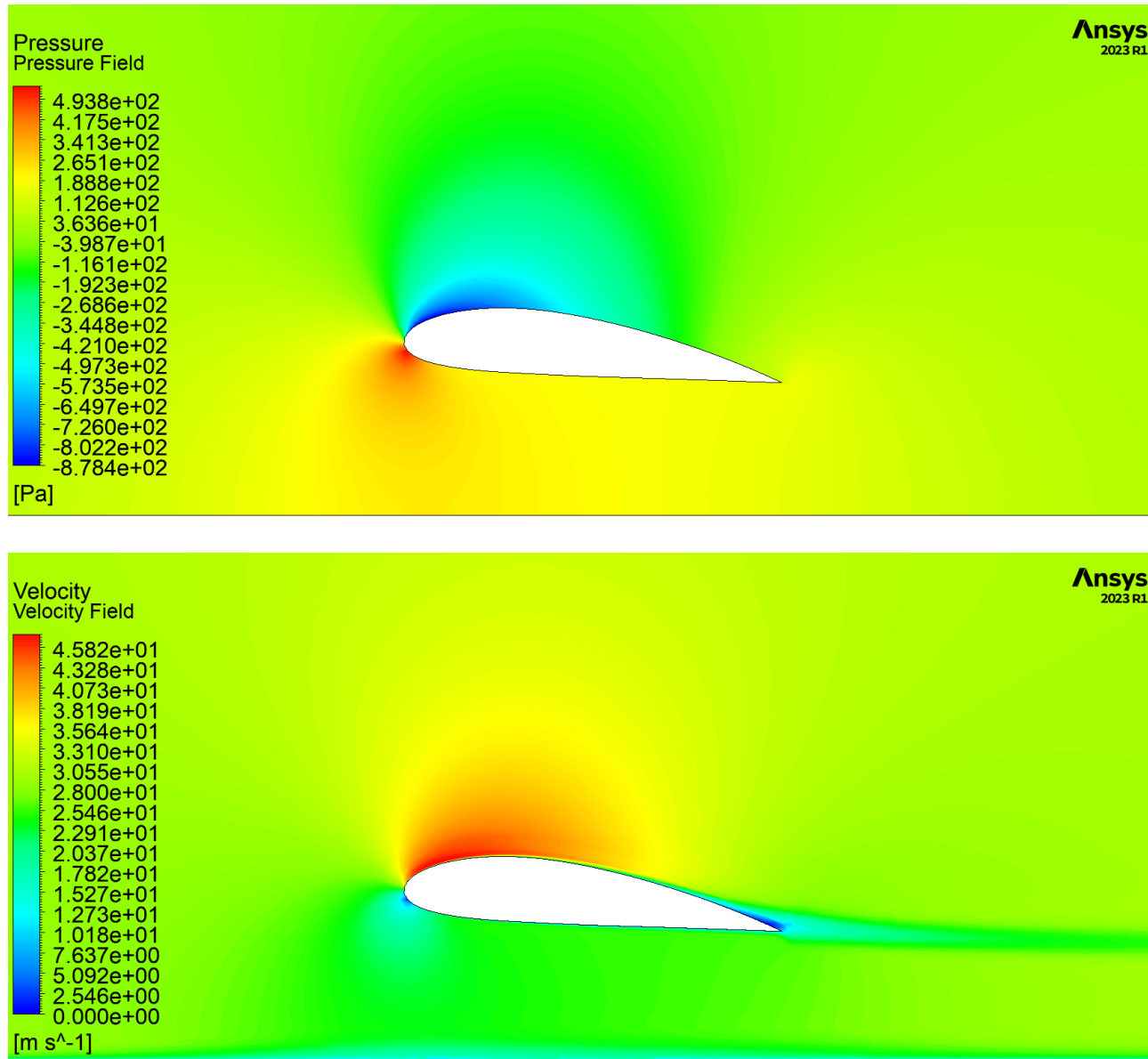


Fig. 7.22 | Contour plots of the pressure and velocity fields around the airfoil at $\alpha = 6^\circ$ and $h/c = 0.4$.

The contour plots are consistent with the results reported by Win *et al.* (2021), confirming the validity of the simulation [3]. The pressure field plot highlights a high-pressure region near the leading edge on the lower surface and a low-pressure region on the upper surface, characteristic of lift generation at a given angle of attack. The velocity field plot shows accelerated flow over the upper surface and decelerated flow on the lower surface, with a distinct wake downstream of the airfoil. These features are indicative of the expected flow behavior around an airfoil in ground effect, further validating the simulation's accuracy.

8 Analysis and conclusions

8.1 Summary of calculated results

h/c	$\alpha = 4^\circ$		$\alpha = 6^\circ$	
	C_L	C_D	C_L	C_D
1	0.894	0.0151	1.094	0.01512
0.8	0.906	0.0144	1.092	0.01442
0.6	0.908	0.0145	1.101	0.01452
0.4	0.921	0.0142	1.127	0.01416
0.2	0.951	0.0136	1.168	0.01361
0.1	0.981	0.0132	1.181	0.01322

Table 8.6 | Aerodynamic coefficients as a function of height-to-chord ratio for $\alpha = 4^\circ$ and $\alpha = 6^\circ$.

8.2 Relevance and accuracy of the results

Returning to the concrete case of our Canadair CL-415, our study presents realistic limitations. The Canadair has a non-zero cabin height, thus our simulation for low flying heights is interesting from an analytical point of view, but cannot be carried out experimentally.

Nevertheless, other experiments have been carried out to study the ground effect on wings similar to NACA 4417. Ahmed *et al.* (2007) obtained experimental results for a 4412 wing in a wind tunnel. For a flight height of $h/c = 1$, and angles of attack of 4° and 6° , the values of the lift coefficient C_L and drag coefficient C_D presented in their Table 2, are quite similar to those found by our simulation [6].

Thus, our study seems to present correct results at the experimental level, or at the simulation level.

8.3 Conclusion

This study investigated the aerodynamic performance of an airfoil in ground effect using numerical simulations conducted in ANSYS Fluent. Through a systematic convergence study, an optimal mesh was selected to balance computational efficiency and accuracy. The lift and drag coefficients were analyzed for various height-to-chord ratios and angles of attack, revealing the influence of ground proximity on aerodynamic forces. The results were validated against existing studies, demonstrating consistency and reliability. These findings contribute to a deeper understanding of ground effect phenomena, with potential applications in the design and optimization of ground-effect vehicles and low-altitude flight systems.

8.4 Recommendations

Future work should extend the range of parameters investigated to gain a more comprehensive understanding of ground effect phenomena. Simulations should encompass a broader spectrum of angles of attack and height-to-chord ratios to generalize the observed trends across different flow conditions. Additionally, the influence of varying Reynolds numbers should be examined to evaluate aerodynamic performance under different operating scenarios. Furthermore, incorporating transient simulations would provide valuable insights into the dynamic behavior of the flow. These simulations could capture unsteady phenomena such as flow separation, wake formation, and temporal variations in lift and drag forces, thereby enhancing the accuracy and applicability of the results to real-world scenarios.

References

- [1] M. Visser, *I-dpcn at work*, Published under CC BY-SA 2.0 terms. [Online]. Available: [https://commons.wikimedia.org/wiki/File:I-DPCN_at_work_03_\(4203528315\).jpg](https://commons.wikimedia.org/wiki/File:I-DPCN_at_work_03_(4203528315).jpg) (cit. on p. 3).
- [2] D. Lednicer, *The incomplete guide to airfoil usage*, Part of the UIUC Airfoil Data Site. [Online]. Available: <https://m-selig.ae.illinois.edu/ads/aircraft.html> (cit. on p. 3).
- [3] S. Y. Win and M. Thianwiboon, “Parametric optimization of naca 4412 airfoil in ground effect using full factorial design of experiment,” *Engineering Journal*, vol. 25, no. 12, pp. 9–19, 2021 (cit. on pp. 5, 23).
- [4] F. M. 101, *Calculators and tools - inflation layer calculator*. [Online]. Available: <https://www.fluidmechanics101.com/pages/tools.html> (cit. on p. 11).
- [5] Q. Qu, W. Wang, P. Liu, and R. K. Agarwal, “Airfoil aerodynamics in ground effect for wide range of angles of attack,” *AIAA Journal*, vol. 53, no. 4, pp. 1048–1061, 2015 (cit. on p. 21).
- [6] M. R. Ahmed, T. Takasaki, and Y. Kohama, “Aerodynamics of a naca4412 airfoil in ground effect,” *AIAA journal*, vol. 45, no. 1, pp. 37–47, 2007 (cit. on p. 24).